Available online at www.sciencedirect.com

jmr&t Journal of Materials Research and Technology

journal homepage: www.elsevier.com/locate/jmrt

Original Article

Corrosion behavior of an Al–Sn–Zn alloy: Effects of solidification microstructure characteristics

André Barros [a,*], Clarissa Cruz [b], Amauri Garcia [a], Noé Cheung [a]

[a] Department of Manufacturing and Materials Engineering, University of Campinas - UNICAMP, 13083-860, Campinas, SP, Brazil

[b] Department of Production Engineering, Federal University of Ouro Preto - UFOP, 35931-008, João Monlevade, MG, Brazil

ARTICLE INFO

Article history:
Received 18 December 2020
Accepted 22 February 2021
Available online 2 March 2021

Keywords:
Solidification
Microstructure
Corrosion resistance

ABSTRACT

Due to its strong influence on service life of manufactured parts, corrosion resistance is an important factor to consider when designing Al alloys for engineering applications. With this in mind, the present study focuses on understanding the role of microstructure features in the corrosion behavior of an Al-10wt.%Sn-5wt.%Zn alloy. Samples with different microstructural length scales were subjected to corrosion tests, which were performed using electrochemical impedance spectroscopy (EIS) and potentiodynamic polarization. An equivalent circuit analysis was also carried out. The results revealed a relatively high electrochemical activity of the studied alloy. Furthermore, coarsening in microstructure showed a slight tendency towards improvements in the corrosion resistance, that is, coarser microstructures composed by Al-rich dendrites surrounded by Sn–Zn constituent particles were comparatively less prone to corrosion degradation than finer ones. Finally, the proposed equivalent circuit model is shown to have good agreement with the experimental EIS measurements.

1. Introduction

Outstanding wear performance, suitable fatigue strength, non-toxicity, and good seizure resistance are some attributes that have rendered Al–Sn alloys attractive for the manufacturing of bearing components used in the automotive industry [1,2] and for use as anodic coatings for anti-corrosive protection of steel [3]. In recent years, some studies have confirmed that the addition of suitable alloying elements is an efficient strategy to improve both the mechanical strength and wear behavior of such alloys [4,5]. However, in order to properly develop multicomponent Al alloys, greater knowledge on their corrosion properties is needed since components may also be exposed to aggressive environments that favor the corrosion process. This especially applies to Al–Sn–Zn alloys, since they are good candidates for use as tribological materials [6–8].

From a physical metallurgy standpoint, one of the most important parameters determining the corrosion behavior

* Corresponding author.
E-mail address: andre.barros13@hotmail.com (A. Barros).

https://doi.org/10.1016/j.jmrt.2021.02.081

of metals and alloys is their microstructure [9]. A literature search reveals evidence that secondary phases formed during solidification and/or thermo-mechanical processing of Al-based alloys exhibit electrochemical characteristics that often differ significantly from the behavior of the Al-rich matrix [10]. Thus, factors like chemical composition, morphology, size, and distribution of the phases forming the alloy microstructure are expected to play a key role in the corrosion resistance [11]. For instance, the microstructure refinement can decrease the corrosion rate of an Al-10wt.%Sn alloy immersed in a 3%NaCl solution, as reported by Osório et al. [12]. These authors also stated that the corrosion resistance of an Al-20wt.%Zn alloy can increase as its microstructure becomes coarser. Regarding Al–Sn–Zn alloys, there is still a lack of studies on the effects of microstructure features on the resulting corrosion properties.

Commonly as-solidified microstructures of Al–Sn–Zn alloys consist of Al-rich dendrites surrounded by Sn-rich particles, with amounts of Zn present in both Al-rich matrix and Sn-rich regions [13]. According to Khireche et al. [14], the presence of Zn/Sn-rich particles at the grain boundaries is a cause of intergranular corrosion in Al-5wt.% Zn-Xwt.%Sn (X = 0.1, 0.2, and 0.4) alloys. The electrochemical interaction among Al, Zn, and Sn-rich phases is also able to form charge transfer and induce severe galvanic corrosion in biodegradable Zn–Al–Sn alloy, as reported by Shuai et al. [15]. On the other hand, a better understanding on how the microstructural length scale affects the corrosion properties of Al–Sn–Zn alloys still remains an essential task to be accomplished. In view of the above considerations, this study aims to investigate the role of microstructure features in the corrosion behavior of an Al-10wt.% Sn-5wt.%Zn alloy solidified under transient heat flow conditions.

2. Experimental procedure

2.1. Solidification experiments

Ten Al-10wt.%Sn-5wt.%Zn alloy samples with distinct thermal histories during solidification were produced from commercial-purity metals (99.9%). Firstly, 850 g of Al were melted in a SiC crucible using a muffle furnace. After complete melting of Al, stoichiometric amounts of Sn and Zn were added to the molten bath, which was then mechanical homogenized. Next, the molten alloy was poured into a stainless-steel mold located inside the casting chamber of a directional solidification device, which is outlined in reference [16]. Real-time temperature monitoring at 7 different positions along the length of the casting was performed using K-type thermocouples connected to a Lynx data acquisition system. When a temperature of 5% above of *liquidus* temperature was measured by the thermocouple closest to the bottom of the mold, all electrical heaters were disconnected from their power source and the water cooling system at the mold bottom-part was activated. Temperature–time data recorded during solidification were used to determine solidification cooling and growth rates ($\dot{T}$ and V_L, respectively) through experimental techniques described previously [17].

2.2. Metallographic examination and chemical analysis

For macrographic characterization, the directionally solidified (DS) casting was sectioned along its vertical axis and one of the half-cylindrical parts was subjected to metallographic grinding with 100- to 1200-grit soft SiC papers. Then, etching with a solution of Kroll's reagent (2 ml of HF, 10 ml of HNO_3, and 88 ml of H_2O) was performed. Next, selected transverse sections of the DS casting at 5, 10, 15, 20, 25, 30, 40, 50, 60, and 70 mm from the cooled bottom were subjected to microstructure characterization. Optical microscopy (Olympus GX41), X-ray diffraction (Panalytical X'Pert PRO MRD XL), and scanning electronic microscopy (ZEISS EVO-MA15) coupled with energy dispersive X-ray spectroscopy (Oxford-XMax) were used. No chemical etching was performed. Using the ImageJ software, primary dendrite arm spacings (λ_1) were measured by means of the linear intercept method [18]. Finally, solutes profiles along the length of the casting were traced by using inductively coupled plasma optical emission spectrometry (Agilent 5100).

2.3. Electrochemical corrosion testing

Using an Autolab PGSTAT128N potentiostat/galvanostat equipped with the NOVA software package, electrochemical impedance spectroscopy (EIS) and potentiodynamic polarization (POL) techniques were performed on samples solidified at $\dot{T}$ values of 1 °C/s (coarser microstructure) and 19 °C/s (finer microstructure), so that two quite different microstructural length scales could be assessed. It is worth mentioning that these samples were extracted from the positions 40 and 5 mm in relation to the cooled bottom of the casting, that is from the position at which $\dot{T}$ reached a quasi-stationary regime and from a selected transverse section associated with a high solidification kinetics, respectively. A conventional three-electrode cell containing an Ag/AgCl 3 M KCl reference electrode, a platinum wire counter electrode, and the Al–Sn–Zn alloy sample under study was used. Corrosion tests were performed in a 0.06 M NaCl solution at room temperature (25 ± 2 °C), with the working electrode circular area that was exposed to the electrolyte solution being of 0.2 cm^2 (0.25-μm diamond paste finishing). It should be mentioned that the use of such diluted saline solution was shown to be appropriate to assess the effects of microstructure coarsening on the corrosion response in previous studies [9,11].

EIS analysis was conducted using a frequency scan from 100 kHz down to 10 mHz (10 points per decade) with an AC signal of 10 mV amplitude in relation to the open-circuit potential (OCP), which was initially recorded during 900 s. In addition, an equivalent circuit analysis was carried out using the NOVA 1.11.0 software. Prior to POL tests, OCP measurements were taken during about 200 s. Finally, POL scans were carried out by stepping the potential at a scan rate of 0.167 mV/s from −250 to 250 mV at OCP. For reproducibly purposes, EIS and POL tests were performed in triplicate.

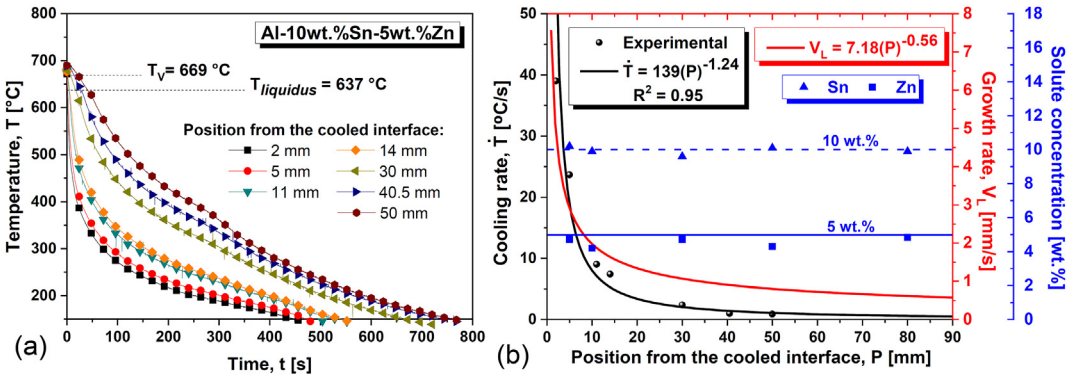

Fig. 1 – (a) Cooling curves recorded along the length of the Al-10wt.%Sn-5wt.%Zn alloy casting during directional solidification; (b) Sn and Zn concentrations, V_L, and $\dot{T}$ profiles from the cooled bottom to the top of the casting.

3. Results and discussion

3.1. *Solidification thermal parameters*

Fig. 1(a) presents temperature–time profiles recorded during solidification of the Al-10wt.%Sn-5wt.%Zn alloy, with each cooling curve referring to a position of thermocouple in relation to the heat-extracting surface at the bottom of the casting. A sharper drop in temperature is noted for thermocouples closer to the cooled bottom of the castings, but this variation in temperature over time decreases progressively towards the inner of the casting. Such behavior can be explained by analyzing Fig. 1(b) in which $\dot{T}$ and V_L are plotted as a function of the relative position in the DS casting. It can be seen that higher values of these thermal parameters are associated with positions near to the cooled bottom of the casting. This can be attributed to the good surface conformity between the solidified shell and the mold surface during the initial stages of solidification. However, as the *liquidus* front advances, both $\dot{T}$ and V_L decrease because of two main reasons: (1) the increase of the thermal resistance related to the solidified shell and (2) the formation of air gaps at the casting/mold interface. As shown in Fig. 1(b), Sn and Zn solutes concentrations along the length of the DS casting remained essentially close to the nominal ones, thus demonstrating absence of macrosegregation. Consequently, both microstructure evolution and corrosion behavior of the studied alloy could be analyzed without the interference of composition variation in the examined DS samples.

3.2. *Correlation between thermal parameters and solidification structures*

Columnar grains aligned along the heat flow direction prevailed along the entire investigated region of the Al–Sn–Zn alloy casting, without trace of columnar-to-equiaxed transition, as can be seen in Fig. 2(a). Representative optical micrographs

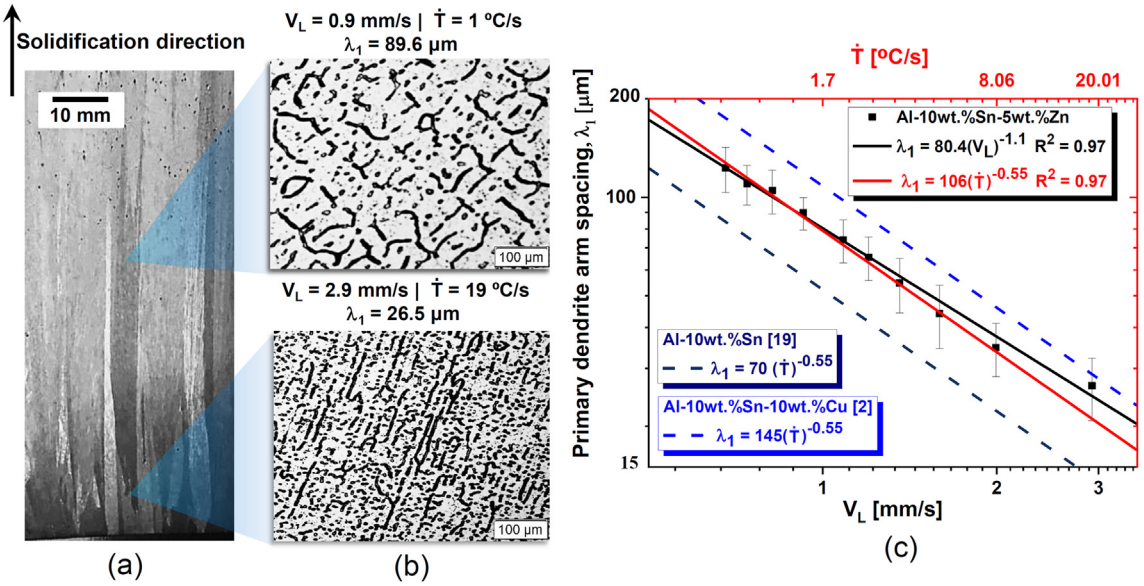

Fig. 2 – (a) Solidification macrostructure; (b) Representative transverse microstructures; (c) Primary dendrite arm spacing as a function of both V_L, and $\dot{T}$.

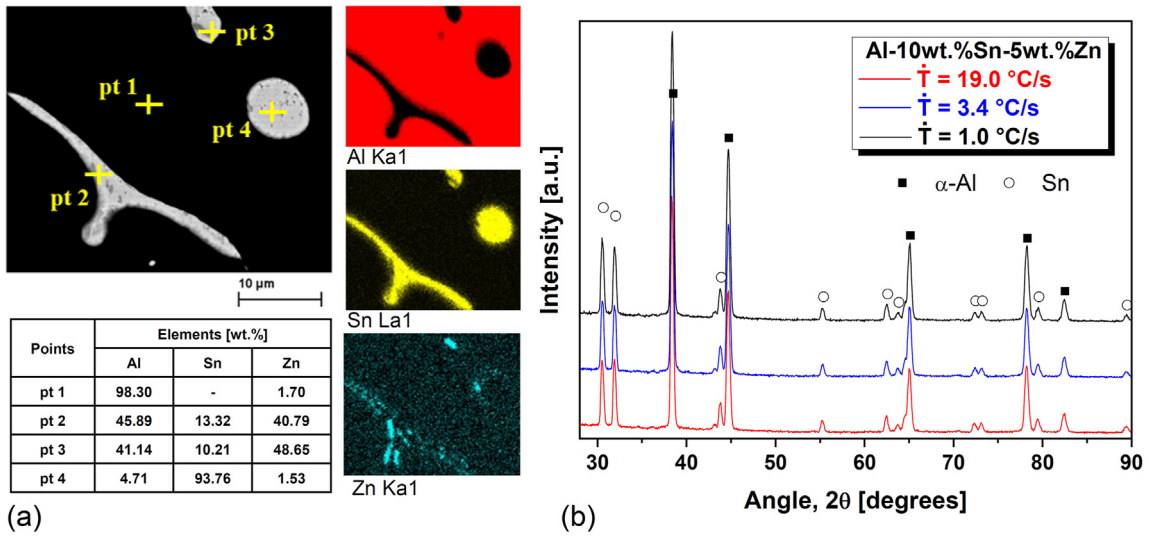

Points	Elements [wt.%]		
	Al	Sn	Zn
pt 1	98.30	-	1.70
pt 2	45.89	13.32	40.79
pt 3	41.14	10.21	48.65
pt 4	4.71	93.76	1.53

Fig. 3 – (a) EDS analysis in a SEM micrograph detailing microstructural phases (b) X-ray diffraction patterns obtained for Al-10wt.%Sn-5wt.%Zn alloy samples solidified at three different cooling rates.

shown in Fig. 2(b) reveal an Al-rich matrix with a dendritic morphology very similar to that previously reported for Al–Sn-(Si; Cu) alloys [2]. This dendritic morphology prevailed along the entire range of cooling rates which was from about 0.5 to 19 °C/s. Fig. 2(c) presents the experimental power laws proposed herein for the growth of primary dendrite arm spacings as a function of solidification thermal parameters, that is, $\lambda_1 = 80.4 (V_L)^{-1.1}$ and $\lambda_1 = 106 (\dot{T})^{-0.55}$. Given that the determination coefficients (R^2) are > 0.9, these equations are able to properly represent the experimental scatter. In order to conduct a comparative analysis with the literature, equations found in previous studies are also plotted [2,19]. It is worth noting that the addition of 5wt.%Zn to the Al-10wt.%Sn alloy promotes increase in λ_1 values for a given $\dot{T}$ value. The rise in λ_1 as a result of third element addition is also observed when such binary Al–Sn alloy is alloyed with 10wt.%Cu.

Fig. 3(a) provides an overview of the SEM/EDS analysis. Note that the dendrites of the pro-eutectic α-Al phase are surrounded by Sn-rich particles while Zn is present in the Al-rich matrix and in Sn-rich particles at the interdendritic regions. By interpreting XRD patterns presented in Fig. 3(b) for samples solidified at different $\dot{T}$ values, only the reflections of α-Al and Sn phases were identified. A possible reason for the absence of the Zn-rich phase in the 2θ peaks is the fact that the particles of such phase occur in such a reduced fraction not detectable by XRD. According to Reyes et al. [20], the non-equilibrium heat flow regime of the solidification experiments is also a possible cause for the absence of the Zn-rich phase in the 2θ peaks of an Al–Bi–Zn alloy. Bayraktar and Hekimoğlu [21] observed that the XRD patterns of binary Al–Zn alloys containing up to 15wt.%Zn reveal the occurrence of only a single-phase microstructure consisting of an Al rich α-phase (solid solution). Thus, by analogy with Al–Zn alloys, it is plausible to assume that no Zn-rich phase will be detectable in the 2θ peaks of the investigated alloy, since the Zn content is 5wt.%.

3.3. *Microstructure features affecting the corrosion behavior*

The EIS data obtained for the investigated samples solidified at cooling rates of 1 °C/s (λ_1 = 89.6 μm) and 19 °C/s (λ_1 = 26.5 μm) are shown in diagrams of Nyquist (Fig. 4(a)) and Bode plots (Fig. 4(b)). By analyzing the Nyquist diagrams, it can be noted a great similarity between the shapes of the curves of both Al–Sn–Zn alloy samples, that is, a capacitive arc at higher frequencies (≥10^4 Hz), an inductive loop at intermediate frequencies (between 10^0 and 10^4 Hz) and, finally, a capacitive arc at lower frequencies (≤10^0 Hz) are identified for finer and coarser microstructures. While the capacitive arc at high frequencies can be attributed to a charge transfer process, the capacitive arc at low frequencies is related to the precipitation of corrosion products. Based on previous investigations [14,22,23], it is plausible to assume that the inductive loop corresponds to pitting corrosion. It can be seen that the magnitude and diameter of the capacitive arc at higher frequencies tend to decrease with decreasing λ_1. At low frequencies it was possible to extract the values of polarization resistance (Rp), which are: 3021 and 3780 Ω cm^2 for samples with λ_1 values equal to 26.5 and 89.6 μm, respectively.

In view of the above analysis, an equivalent circuit for modeling the EIS data is proposed, as depicted in Fig. 4(c). It was slightly modified from the ones proposed by Liu et al. [22] and Sun et al. [23]. The quality of the experimental/simulated fit was evaluated by chi squared (χ^2) values. In this circuit, R_1 is the electrolyte resistance, CPE_1 represents the double layer capacitance, R_2 is the charge transfer resistance, R_3 and L are the corresponding parameters for pitting. CPE_2 is placed in parallel with R_4, and then in series with CPE_3 to represent the capacitive loop, which is related to the precipitation of corrosion products. Table 1 summarizes the values of all equivalent circuit elements used in the simulation according to the proposed model. It can be seen that lower values of R_2,

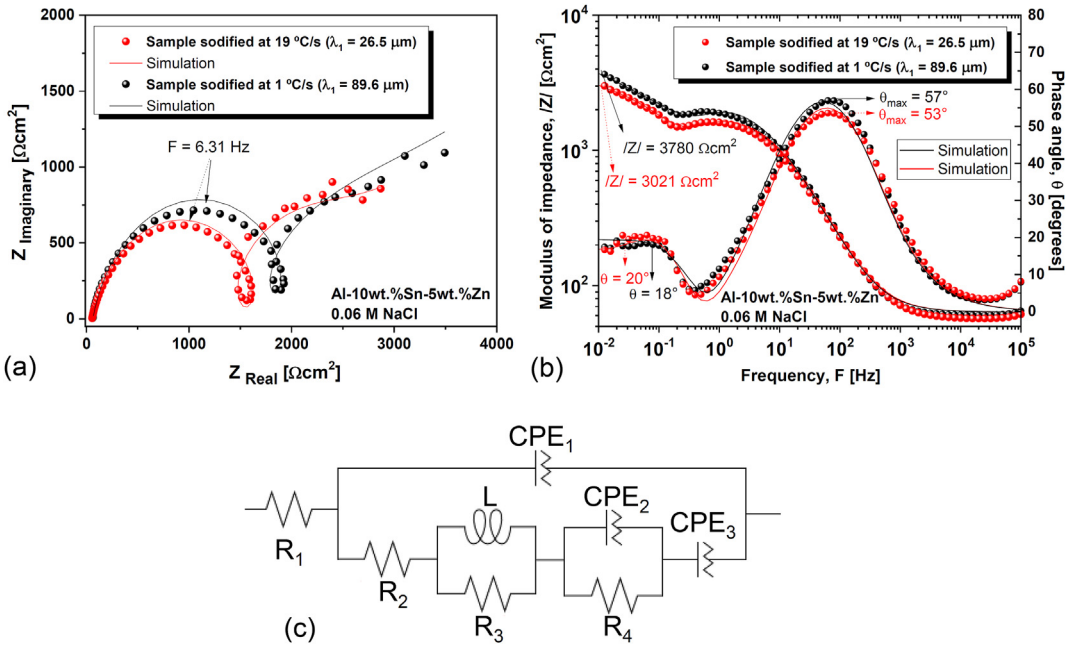

Fig. 4 – Experimental and simulated EIS diagrams of Al-10wt.%Sn-5wt.%Zn alloy in 0.06 NaCl solution for two different microstructural length scale: (a) Nyquist and (b) Bode representations; (c) Equivalent circuit proposed herein.

Table 1 – EIS parameters of Al-10wt.%Sn-wt.%5Zn alloy with two different microstructural length scales.

EIS parameter	Sample solidified at 19 °C/s ($\lambda_1 = 26.5$ μm)	Sample solidified at 1 °C/s ($\lambda_1 = 89.6$ μm)
R1 (Ωcm^2)	63.70	63.70
R2 (Ωcm^2)	0.901×10^3	0.999×10^3
R3 (Ωcm^2)	0.715×10^3	0.862×10^3
R4 (Ωcm^2)	1.078×10^3	1.176×10^3
CPE 1 (μMho/cm^2)	21.94	21.94
n_1	0.834	0.837
CPE 2 (μMho/cm^2)	1.974×10^3	1.785×10^3
n_2	0.822	0.638
CPE 3 (μMho/cm^2)	2.413×10^3	1.151×10^3
n_3	0.389	0.367
L (Hcm^2)	196	196
χ^2	9×10^{-3}	5×10^{-3}

R_3, and R_4 are obtained for tests conducted with the sample having finer microstructure. This suggests that the corrosion processes of charge transfer, pitting, and products precipitation tend to accelerate as the microstructure becomes more refined.

Fig. 5(a) shows the polarization curves, that is, electrochemical potential as a function of current density. No passive region is exhibited in both curves. Besides, an abrupt increase in the anodic current densities is identified for both samples, thus characterizing the relatively high electrochemical activity of the studied alloy, with the corrosion potentials (E_{Corr}) being considered equal to those of nucleation and evolution of pits. In order to obtain i_{corr}, Tafel's extrapolation was used. The lowest corrosion current density ($i_{Corr} = 2.5$ μA/cm^2) was attained for the sample solidified at lower cooling rate ($\lambda_1 = 89.6$ μm) and it was shown to be associated with an E_{Corr} value of − 1.06 V. On the other hand, the highest i_{corr} (3 μA/cm^2) was found for the sample solidified at higher cooling rate ($\lambda_1 = 26.5$ μm) and it was shown to be associated with an E_{Corr} value of − 1.08 V. These observations are in agreement with the results of the EIS analysis, thus confirming that microstructure refinement shows a slight tendency towards decrease in the corrosion resistance.

Concerning experimental results of other multicomponent Al alloys immersed in a 0.06 M NaCl solution, Brito et al. [11] reported values of i_{Corr} and E_{Corr} varying from 0.0346 to 0.432 μA/cm^2 and from −0.726 to −0.650 V, respectively, for an Al-3wt.%Mg-1wt.%Si alloy. Rodrigues et al. [24] reported values of i_{Corr} and E_{Corr} varying from 0.088 to 1.2 μA/cm^2 and from −0.548 to −0.540 V, respectively, for an Al-15wt.%Cu-1wt.%Ni alloy. As can be seen, the investigated Al–Sn–Zn alloy shows a high electrochemical activity when compared to the Al–Mg–Si and Al–Cu–Ni alloys since the i_{Corr} and E_{Corr} values found in the present study are higher and lower, respectively, than those previously reported in the literature. Additionally, in the works carried out by Brito et al. [11] and Rodrigues et al. [24] the microstructure refinement was reported to increase the corrosion resistance. However, the results obtained herein indicate that the microstructure refinement can promote the opposite in Al–Sn–Zn alloys.

Fig. 5(b) shows a representative SEM micrograph of the studied alloy after polarization measurements, along with the

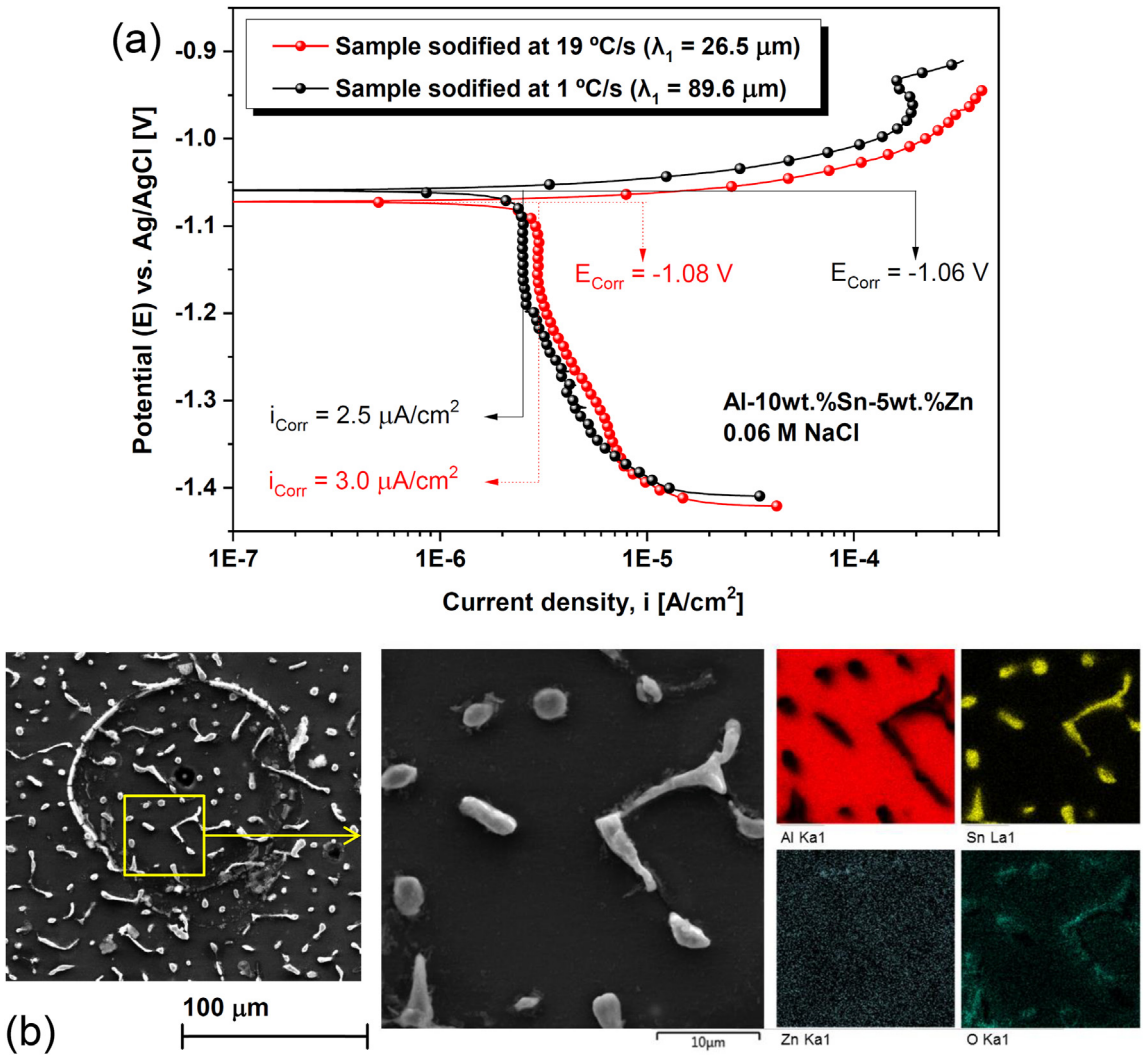

Fig. 5 – (a) Potentiodynamic polarization curves of Al-10wt.%Sn-5wt.%Zn alloy for two different lengths of microstructure scale; (b) Typical SEM image of studied samples after electrochemical corrosion testing.

EDS elemental mapping. It is worth noting that oxygen is present in the matrix areas surrounding the Sn-rich particles within the interdendritic contours, thus suggesting that such Sn-rich constituents are nobler particles and exhibit high efficiency for supporting oxygen reduction than the Al-rich matrix. According to Khireche et al. [14], since Zn is more electronegative than Al and Sn, it is plausible to assume that it may be dissolved in anodic potentials. These authors also stated that the microstructural arrangement formed during solidification favors the formation of galvanic cells Sn(Zn)/Al, which in presence of Cl^- ions increase the dissolution process of Zn as compared to Sn.

4. Conclusions

The following conclusions can be drawn from the present study:

(1) A dendritic morphology was shown to prevail for the pro-eutectic α-Al phase in a broad range of solidification cooling rates, and experimental expressions for the growth of the primary dendrite arm spacing as a function of V_L, and $\dot{T}$ during solidification of the Al-10wt.% Sn-5wt.%Zn alloy are proposed.

(2) The studied Al–Sn–Zn alloy showed a relatively high electrochemical activity. An abrupt increase in the anodic current densities was shown to occur and no passive region in the polarization curves has been observed.

(3) The alloy microstructural length scale was found to have an influence on the corrosion performance of the Al-10wt.%Sn-5wt.%Zn alloy. Higher cooling and growth rates decreased the primary dendrite arm spacings, which resulted in a slight tendency towards the decrease in the corrosion resistance.

Declaration of Competing Interest

The authors declare that they have no known competing financial interests or personal relationships that could have appeared to influence the work reported in this paper.

Acknowledgments

This work was supported by CNPq - National Council for Scientific and Technological Development (grant: 140918/2018–3). Authors also acknowledge LNANO - Brazilian Nanotechnology National Laboratory for the use of the X-ray diffractometer.

REFERENCES

[1] Liu X, Zeng MQ, Ma Y, Zhu M. Wear behavior of Al–Sn alloys with different distribution of Sn dispersoids manipulated by mechanical alloying and sintering. Wear 2008;265(11–12):1857–63.
[2] Bertelli F, Brito C, Ferreira IL, Reinhart G, Nguyen-Thi H, Mangelinck-Noël N, et al. Cooling thermal parameters, microstructure, segregation and hardness in directionally solidified Al-Sn-(Si;Cu) alloys. Mater Des 2015;72:31–42.
[3] Makhatha ME, Fatoba OS, Akinlabi ET. Effects of rapid solidification on the microstructure and surface analyses of laser-deposited Al-Sn coatings on AISI 1015 steel. Int J Adv Manuf Technol 2018;94(1–4):773–87.
[4] Bertelli F, Freitas ES, Cheung N, Arenas MA, Conde A, Damborenea J, et al. Microstructure, tensile properties and wear resistance correlations on directionally solidified Al-Sn-(Cu;Si) alloys. J Alloys Compd 2017;695:3621–31.
[5] Lu ZC, Gao Y, Zeng MQ, Zhu M. Improving wear performance of dual-scale Al–Sn alloys: the role of Mg addition in enhancing Sn distribution and tribolayer stability. Wear 2014;309(1–2):216–25.
[6] Gerashchenkov DA, Sobolev MY, Markov MA, Gerashchenkova EY, Bykova AD, Krasikov AV, et al. Tribolical study of cermet coatings Al–Sn–Zn–Al2O3 for friction couples. J Frict Wear 2018;39(6):522–7.
[7] Abu-Zeid OA. Tribology and corrosion of Al-1.5wt.%Zn-5wt.% Sn ion platings. Wear 1990;139(2):313–8.
[8] Rusin NM, Skorentsev AL. Macrostructure and strength of the Al–Zn–Sn composite produced by liquid-phase sintering of the al–zn alloy and pure tin powder mixture. Russ J Non-Ferrous Metals 2019;60(3):295–300.
[9] Septimio RS, Arenas MA, Conde A, Garcia A, Cheung N, Damborenea JD. Correlation between microstructure and corrosion behaviour of Bi-Zn solder alloys. Corrosion Eng Sci Technol 2019;54(4):362–8.
[10] Birbilis N, Buchheit RG. Electrochemical characteristics of intermetallic phases in aluminum alloys: an experimental survey and discussion. J Electrochem Soc 2005;152(4):B140–51.
[11] Brito C, Vida T, Freitas E, Cheung N, Spinelli JE, Garcia A. Cellular/dendritic arrays and intermetallic phases affecting corrosion and mechanical resistances of an Al–Mg–Si alloy. J Alloys Compd 2016;673:220–30.
[12] Osorio W, Spinelli J, Cheung N, Garcia A. Secondary dendrite arm spacing and solute redistribution effects on the corrosion resistance of Al-10wt%Sn and Al-20wt%Zn alloys. Mater Sci Eng, A 2006;420:179–86.
[13] Zhang F, Edalati K, Arita M, Horita Z. Hydrolytic hydrogen production on Al–Sn–Zn alloys processed by high-pressure torsion. Materials 2018;11(7):1209.
[14] Khireche S, Boughrara D, Kadri A, Hamadou L, Benbrahim N. Corrosion mechanism of Al, Al–Zn and Al–Zn–Sn alloys in 3 wt.% NaCl solution. Corrosion Sci 2014;87:504–16.
[15] Shuai C, Xue L, Gao C, Peng S, Zhao Z. Rod-like eutectic structure in biodegradable Zn-Al-Sn alloy exhibiting enhanced mechanical strength. ACS Biomater Sci Eng 2020;6:3821–31.
[16] Soares T, Cruz C, Barros A, Garcia A, Cheung N. Microstructure growth morphologies, macrosegregation, and microhardness in Bi–Sb thermal interface alloys. Adv Eng Mater 2020;22:1901592.
[17] Cruz C, Lima T, Kakitani R, Barros A, Garcia A, Cheung N. Plate-like growth in a eutectic Bi–Ni alloy: effects of morphological microstructure evolution and Bi3Ni intermetallic phase on tensile properties. Journal of Materials Research and Technology 2020;9(3):4940–50.
[18] Gündüz M, Çadırlı E. Directional solidification of aluminium–copper alloys. Mater Sci Eng, A 2002;327(2):167–85.
[19] Oliveira R, Costa TA, Dias M, Konno C, Cheung N, Garcia A. Transition from high cooling rate cells to dendrites in directionally solidified Al-Sn-(Pb) alloys. Materials Today Communications 2020;25:101490.
[20] Reyes R, Casteletti L, Garcia A, Spinelli J. Characterization of microstructure and wear resistance of a monotectic Al-Bi-Zn alloy. J Phys Chem Solid 2020;147:109631.
[21] Bayraktar S, Hekimoğlu A. Effect of zinc content and cutting tool coating on the machinability of the Al-(5–35) Zn alloys. Met Mater Int 2020;26:477–90.
[22] Liu F, Zhang J, Sun C, Yu Z, Hou B. The corrosion of two aluminium sacrificial anode alloys in SRB-containing sea mud. Corrosion Sci 2014;83:375–81.
[23] Sun H, Liu L, Li Y, Ma L, Yan Y. The performance of Al–Zn–In–Mg–Ti sacrificial anode in simulated deep water environment. Corrosion Sci 2013;77:77–87.
[24] Rodrigues A, Lima T, Vida T, Brito C, Garcia A, Cheung N. Microstructure and tensile/corrosion properties relationships of directionally solidified Al–Cu–Ni alloys. Met Mater Int 2018;24:1058–76.